OAK RIDGE
NATIONAL LABORATORY
MANAGED BY UT-BATTELLE
FOR THE DEPARTMENT OF ENERGY

ORNL/TM-2014/446

Light Water Reactor Sustainability

Baseline Characterization of Cast Stainless Steels

September 2014

Prepared by:

T. S. Byun and Y. Yang

Oak Ridge National Laboratory

UT-BATTELLE
ORNL-27 (4-00)

ORNL/TM-2014/446

Light Water Reactor Sustainability

Milestone #: LW-140R0402152

Baseline Characterization of Cast Stainless Steels

Thak Sang Byun
Ying Yang
Chinthaka M. Silva
Eric T. Manneschmidt
Ronald L. Swain

Materials Science & Technology Division
Oak Ridge National Laboratory

Date Published: September 2014

Prepared under the direction of the
U.S. Department of Energy
Office of Nuclear Energy
Light Water Reactor Sustainability
Materials Aging and Degradation Pathway

Prepared by:
OAK RIDGE NATIONAL LABORATORY
Oak Ridge, Tennessee 37831-6283
managed by
UT-BATTELLE, LLC
for the
U. S. DEPARTMENT OF ENERGY
under contract DE-AC05-00OR22725

CONTENTS

Page

CONTENTS ..... **V**

1. EXECUTIVE SUMMARY **1**

2. MATERIALS AND MICROSTRUCTURE **3**

2.1. CHEMISTRY 3
2.2. MICROSCOPIC CHARACTERISTICS 4

3. MECHANICAL CHARACTERIZATION **8**

3.1 TENSILE TESTING 8
3.2 CHARPY IMPACT TESTING 9
3.3 STATIC FRACTURE TESTING 9
3.3.1. Preparation of fracture specimens *9*
3.3.2. Simplified data acquisition *10*
3.3.3. Static fracture testing *11*
3.4 ANALYSIS OF FRACTURE TEST DATA 11
3.4.1. Calculation of load-'plastic' displacement data *11*
3.4.2. Calculation of J-integral *12*
3.4.3. Calculation of normalized load-displacement data *13*
3.4.4. Construction of J-R curve and determination of fracture toughness *14*

4. RESULTS OF MECHANICAL TESTING AND EVALUATION **14**

4.1 TENSILE STRENGTH AND DUCTILITY 14
4.2 TRANSITION BEHAVIOR OF CHARPY IMPACT ENERGY 17
4.3 STATIC FRACTURE BEHAVIOR AND ITS TEMPERATURE DEPENDENCE 18

5. COMPUTATIONAL STUDY ON PRECIPITATE PHASES **23**

5.1. CALCULATION METHOD AND CONDITIONS 23
5.2. PRECIPITATION BEHAVIORS 24

6. SUMMARY & CONCLUSION **28**

REFERENCES **29**

BASELINE CHARACTERIZATION OF CAST STAINLESS STEELS

Thak Sang Byun, Ying Yang, Chinthaka M. Silva, Eric T. Manneschmidt, Ronald L. Swain
Oak Ridge National Laboratory

1. EXECUTIVE SUMMARY

This research aims to build a systematic knowledge base for the thermal aging behavior of cast stainless steels (CASSs) that can be used to draw conclusive predictions for the integrity of the CASS components of LWR power plants during the extended service life up to and beyond 60 years [1]. Mechanical and microstructural data obtained through accelerated aging experiment and computational simulation will be the key data for the prediction of CASS behaviors.

In this fiscal year, various mechanical tests have been performed to obtain baseline property data for the four model alloys, CF3, CF3M, CF8, and CF8M, in pristine condition, including tensile property, Charpy impact, and fracture toughness and resistance data. Chemical analysis and basic microstructural observation were also performed for the same alloys. In addition, preliminary CALPHAD calculations for phase stability and precipitation behavior in CASSs were performed based on the microscopy data and assumption of equilibrium composition distribution. Summarized below are the results of these baseline tests and analyses:

- The ferrite volume fractions measured for the CF3 and CF8 alloys were 7.9 and 6.7%, respectively; slightly higher volume fractions, 11.8 and 11.6%, were measured for the CF3M and CF8M alloys with more Mo content. EDS maps showed that elemental partitioning existed between ferrite (Cr and Mo enriched) and austenite (Ni enriched) while Fe distribution appeared to be relatively uniform over the two phases.
- In the temperature range -100 to 400 °C both ductility and strength decreased with test temperature. Very high tensile strength (>800 MPa) and high total ductility (>70%) were measured at -100 ºC, which might be because of highly linear dislocation slip with formation of twins and martensite particles. In aging temperature region (290–400 ºC) both the strength and the ductility were not highly temperature dependent, which indicated that the same deformation mechanism was activated at the elevated temperatures.
- The impact energy of model alloys showed clear but wide transition region in the test temperature range, -196 to 100 ºC; however, the lower shelf of absorbed energy was not formed as the lowest test temperature was still within the transition region. The upper shelf energy was observed at 0–100 ºC for CF3, CF8, and CF8M, but not for CF3M, which showed excessive plasticity at 100 ºC and yielded a 'no test' case. Therefore, the ductile-brittle transition temperature (DBTT) could not be defined due to too high absorbed energy. Instead, a new parameter T_{100J} was defined to guarantee existence of a value; it was determined at -125, -143, -118, and -175 ºC, for CF3, CF3M, CF8, and CF8M, respectively.
- Over the whole test temperature range, -175 to 400 ºC, no fracture toughness below 200 MPa√m was measured from the model CASS materials. For each of these alloys, peak fracture toughness was observed at RT or -100ºC, below which K_{JQ} decreased with temperature but

never reached brittle or lower shelf region. Variation of fracture toughness in the aging temperature region (290–400ºC) was not significant, which might be because of the near constant strength and ductility in the region.

- CALPHAD calculation has predicted several key precipitation behaviors: The G-phase formation is strongly dependent on aging temperature and is relatively enhanced in the CF3M and CF8 alloys. The Fe_2Mo Laves phase forms preferably in the high Mo alloys, CF3M and CF8M. The π-phase formed in the alloys with high Mo contents at the lowest aging temperature (290 ºC) only. The simple nitride (Cr_2N) and common carbide ($M_{23}C_6$) formed in all model alloys, with a weak dependence on aging temperature.

2. MATERIALS AND MICROSTRUCTURE

The characterization performed in the fiscal year 2014 was to obtain baseline data for the four model alloys of CF3, CF3M, CF8, and CF8M, which will be used as reference data to measure aging effects and as input dada for computational simulation. Chemical analysis and basic microstructural observation have been performed first for the alloys, and the results are summarized in this section, along with the procedures.

2.1. Chemistry

Two chemistry data sets were provided by the alloy producer, Stainless Foundry & Engineering Inc, Milwaukee, WI (Table 1) and by an independent party, Dirats Laboratories, Westfield, MA (Table 2). Listed in Table 2 are the detailed chemistry data obtained for the model alloys and will be used as official chemistries for the future researches and publications. As noted in the chemical compositions, the major compositions of CASSs such as Fe, Cr, Ni, Mn, Mo, Si, C are within the specifications of respective alloys, while the contents of minor elements such as S and N were higher than required for some alloys. In particular, the N contents are consistently higher than the limit of 0.5% in the specification. However, the effect of the excessive N content was not examined since the difference between alloys was limited.

Table 1. Ingot Chemistry (wt.%) form the Stainless Foundry & Engineering Inc. (2014 Feb)

Grade	Fe	Cr	Ni	Mn	Mo	Si	P	C	S
CF3 (304L)	Bal.	18.7	8.1	1.37	0.34	1.25	0.033	0.02	0.034
CF3M (316L)	Bal.	19.1	9.9	1.16	2.3	1.20	0.033	0.02	0.022
CF8 (304)	Bal.	18.5	8.5	1.08	0.29	1.26	0.032	0.05	0.025
CF8M (316)	Bal.	18.6	10.0	0.72	2.3	1.04	0.032	0.05	0.026

Table 2. Official Chemistry (wt.%) performed at Dirats Laboratories (2014 May)

Grade	Fe	Cr	Ni	Mn	Mo	Si	Cu	Co
CF3	Bal.	19.17	8.11	1.44	0.34	0.99	0.41	0.18
CF3M	Bal.	19.28	9.81	1.14	2.30	1.22	0.28	0.15
CF8	Bal.	18.72	8.91	1.10	0.29	1.27	0.29	0.15
CF8M	Bal.	18.52	10.38	0.65	2.33	1.02	0.33	0.17

Table 2. (continued)

Grade	V	W	P	C	S	O	N	Block
CF3	0.07	0.04	0.029	0.026	0.032	0.020	0.102	CF3b
CF3M	0.05	0.02	0.033	0.028	0.025	0.022	0.084	CF3Ma
CF8	0.05	0.03	0.026	0.067	0.038	0.016	0.061	CF8a
CF8M	0.06	0.04	0.031	0.043	0.024	0.021	0.102	CF8Mb

2.2. Microscopic characteristics

Microscopic characterization data including optical grain structure and SEM-EDS map data have been obtained to measure the volume fractions of austenite and ferrite phases and to confirm existence of these phases using elemental distribution maps.

Samples of the model alloys were etched with Glyceregia solution (30 ml glycerol, 30 ml HCl, 10 ml HNO_3) to reveal the duplex grain structure, as shown in Fig.1. Glyceregia is known to attack and reveal grain boundary, ferrite and sigma phases, and high carbide/carbon area in austenitic steels and austenitic-ferritic duplex steels [2], which results in slightly darker ferrite area compared to the austenite area. Volume fractions were measured with linear intercept method to help explaining the mechanical properties as well as to provide input for the computational analysis on phase stability and precipitation.

The volume fractions of delta ferrite were 7.9 and 6.7% for CF3 and CF8, and 11.8 and 11.6% for CF3M and CF8M, respectively. It is noted that CF3M and CF8M, which contain relatively higher Mo content, have higher amount of ferrite, as is known as a ferrite former or ferrite stabilizing element. The volume fractions of CF3 and CF8 are relatively lower than the typical level known for nuclear grade CASSs. In general, the nuclear grade CF3 and CF3M can contain a wide range of ferrite, 3 to 30%, in an austenite matrix, although the CF3 alloys typically contain 10 to 20 percent ferrite [1,3-10]. The amount of ferrite varies strongly with composition and with ingot production. In the present cases, a high rate cooling due to small ingot size (~10 cm in diameter) may be the cause of low ferrite formation in CF3 and CF8. It is also known that a higher ferrite content generally leads to higher tensile strength, which indicates the strength of these model alloys are within narrow range [3,7].

The formation of delta ferrite is controlled by the conditions of solidification process, and therefore, its morphology and volume fraction are known to vary with the chemical composition of cast alloy and size of casting [7]. Regardless of some differences found in the details of microstructures, Figure 1 compares similar ferrite morphologies, all of which combine globular, acicular, and lacy ferrite islands. The acicular morphology is characterized by fine needle-like ferrite that is distributed in the austenite matrix. Ferrite morphology is globular for materials containing <5% ferrite while it becomes interconnected network of elongated ferrite islands, or a lacy morphology, as the ferrite volume increases [7]. Since the ferrite phase forms preferably along the austenite grain boundaries (see Fig. 2), an enough amount of ferrite can, ideally, form a complete or near-complete network covering most of grain boundaries and enclosing austenite grains. Figure 1 indicates that no model CASS has a volume fraction of > ~ 25%, above which the ferrite phase would show contiguity along grain boundaries and show a steep change in mechanical behaviors.

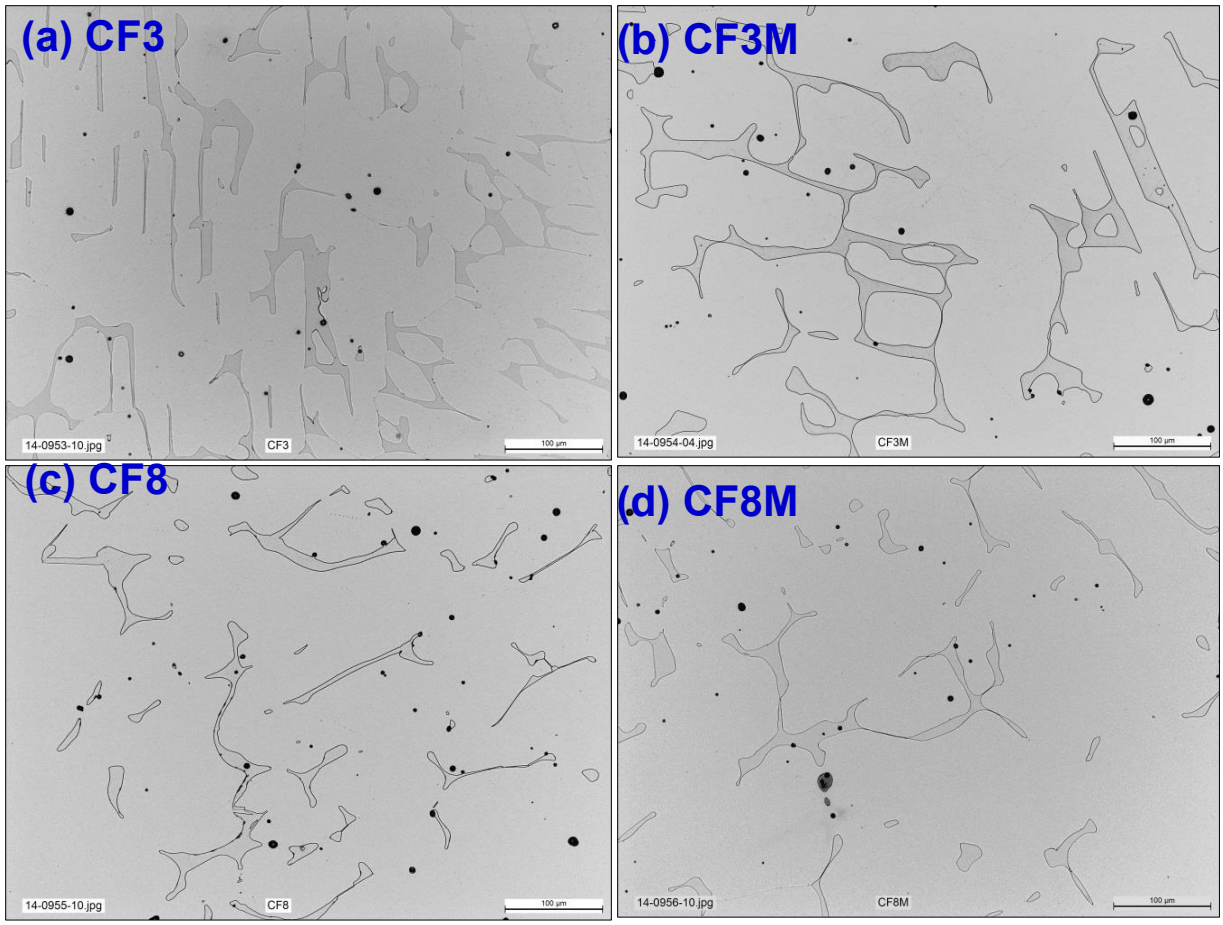

Figure 1. Optical micrographs for the model cast stainless steels, (a) CF3, (b) CF3M, (c) CF8, and (d) CF8M, showing various ferrite (darker phase) morphologies.

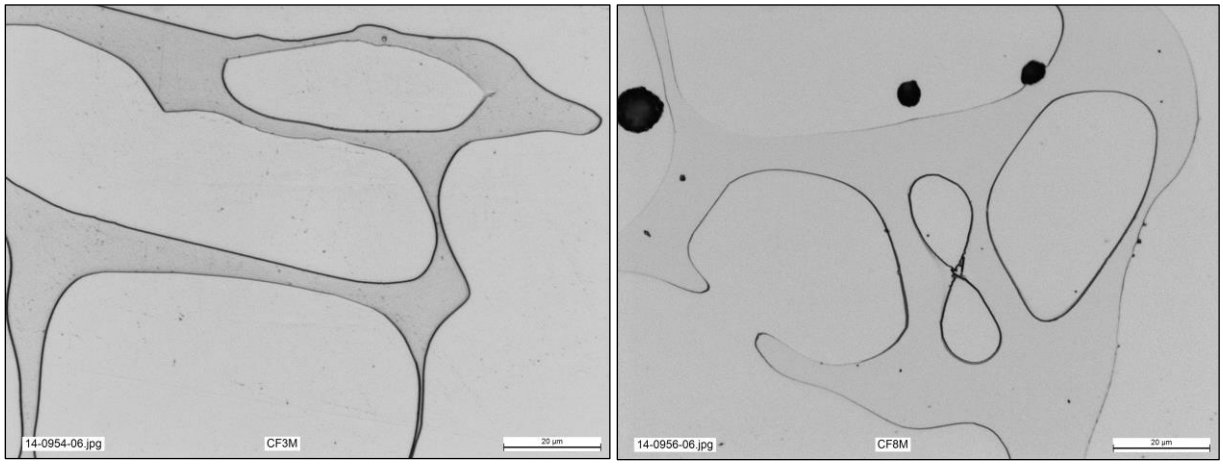

Figure 2. Two ferrite/austenite duplex morphologies showing the details of formation of network in CF3M (left) and CF8M (right)

Various SEM functions have been utilized to characterize the formation behavior and morphology of delta ferrite. First, Figure 3 displays energy-dispersive X-ray spectroscopy (EDS) maps obtained for a ferrite-austenite area in the CF8M. These EDS maps clearly demonstrate elemental partitioning between ferrite (Cr & Mo enriched) and austenite (Ni enriched). Such partitioning in elemental distribution should be subjected to the relative diffusion rates of individual chemical elements during solidification, and therefore this result is an evident for the ferrite formation being dependent on cooling rate or ingot size. The map for Fe indicates that the distribution of Fe is relatively uniform.

As compared in Table 3, the volume fractions were also measured from the EDS images as we could measure the Cr-enriched area for ferrite phase and the Ni-enriched area for austenite area. With this technique, however, area-to-area fluctuation was too large to be used as an average value. Therefore, the volume fraction data measured from the optical micrographs will be used as official data. Comparing the ferrite contents from optical images, it is obvious that the Mo content is the most influential parameter determining resultant volume fraction. This may be because Mo is the heaviest element among the major alloying elements and thus its diffusion should be slowest or rate-controlling. Therefore, the most effective method to increase ferrite content would be increasing the Mo content.

Second, the electron back scattering diffraction (EBSD) images were obtained to confirm the ferrite morphology, along with the optical micrographs. Figure 4 displays the EBSD images for the present model cast stainless steels. Note that these phase maps look grainy because some complications exist in both texture and strain, and because the large area (>60,000 square micrometers) has to be scanned at a relatively high speed due to the coarse microstructure. Figure 4 clearly show the ferrite phase islands in austenite matrix, mostly along grain boundaries.

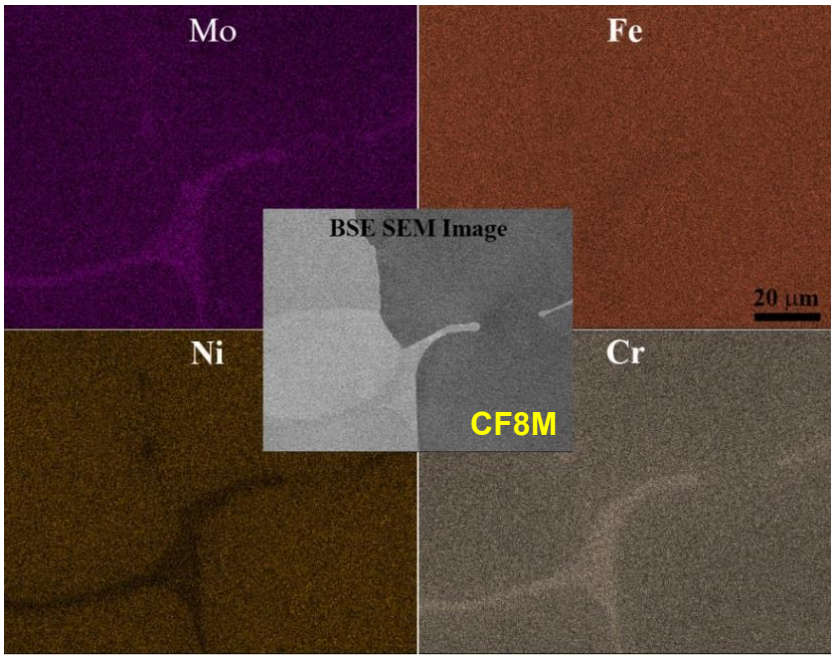

Figure 3. EDS maps showing elemental partitioning between ferrite (Cr & Mo enriched) and austenite (Ni enriched).

Table 3. Summary of volume fraction measurements

CASS ID	Ferrite (%) in a EDS Cr-map	Ferrite (%) in Optical Image
CF3	17.5	7.9
CF3M	5.1	11.8
CF8	3.7	6.7
CF8M	7	11.6

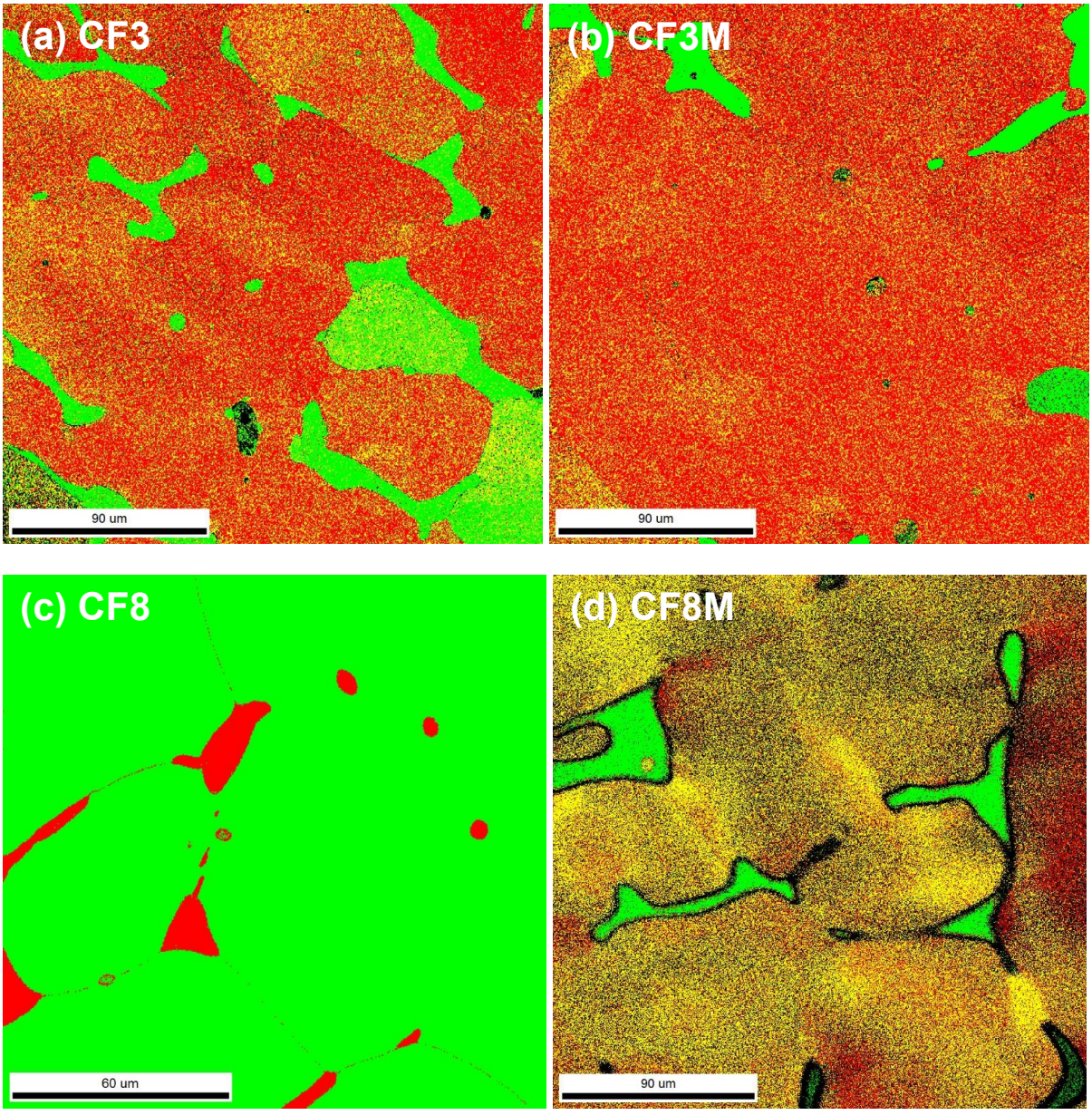

Figure 4. EBSD images for the model cast stainless steels, which clearly show ferrite phase islands in austenite matrix, mostly along grain boundaries.

3. MECHANICAL CHARACTERIZATION

This chapter describes mechanical testing procedures and test results. In this fiscal year mechanical tests were performed to obtain mechanical property data for the four model alloys in pristine condition. These mechanical data include tensile property data, Charpy impact energy data, and fracture toughness and fracture resistance data, which will be used as baseline data to evaluate aging effect in terms of these properties. As described in this chapter, the tasks of this year also aimed to establish testing methods, which can be used in future tests for aged and pre-aged materials.

3.1 Tensile testing

The SS-3 dogbone type specimen with a gage section of 7.62×1.52×0.76 mm^3 was used for the tensile testing. All tensile specimens were machined to have their length direction perpendicular to the longitudinal direction of the ingot (near T-orientation). Tensile tests were performed in two MTS servohydraulic testing systems with 2.2 kN load cell and equipped, respectively, with heating and cooling capabilities. Test temperatures were in the range of -100 ℃ to 400 ℃, which include all aging temperatures: 290, 330, 360, and 400 ℃. All tensile tests were performed using a shoulder loading method at a displacement speed of 0.46 mm/min, which corresponds to a nominal strain rate of 0.001 s^{-1} at the gage section of specimen. For the temperature control, an infrared light furnace and a liquid-nitrogen injection system were used for heating and cooling in air, respectively. Data acquisition rate in recording time, stroke, and load was 10 points per second, and the raw data were analyzed for determining engineer data including yield and tensile stresses, and uniform and total elongations. Both test procedure and data treatment followed the standard method in ASTM E8 [11]: 'Standard Test Method for Tension Testing of Metallic Materials.'

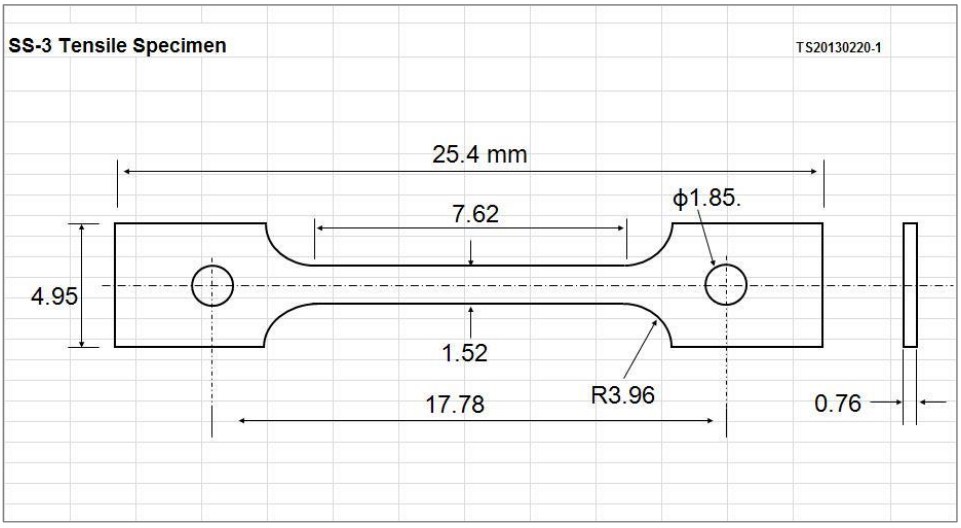

Figure 5. SS-3 subsize tensile specimen

3.2 Charpy impact testing

The standard Charpy specimen, a notched square bar of 10×10×55 mm^3 with 2 mm deep notch, was used for the impact testing [12]. Impact tests were carried out in a 300 J capacity Tinius-Olsen machine with temperature control by a heating-cooling chamber. Test temperatures were chosen to surely include the transition temperatures of the model alloys: the same range of test temperature, -175 to 100ºC, was applied to all sets of specimens unless the specimen started to experience jamming due to excessive plasticity. The impact energy of CASS model alloys before aging was expected to reach upper shelf around room temperature or 100ºC. The lower shelf indicating brittle failure, however, was not expected to be observed in the test temperature range due to the characteristic low temperature ductility of stainless steels. The specimen temperature was measured by a thermocouple embedded in the dummy specimen that was set on the top of the test specimen until the temperature reading stabilized. The thermocouple was then removed before releasing the striker. In testing the swing speed measured at the striker was ~5.4 m/s.

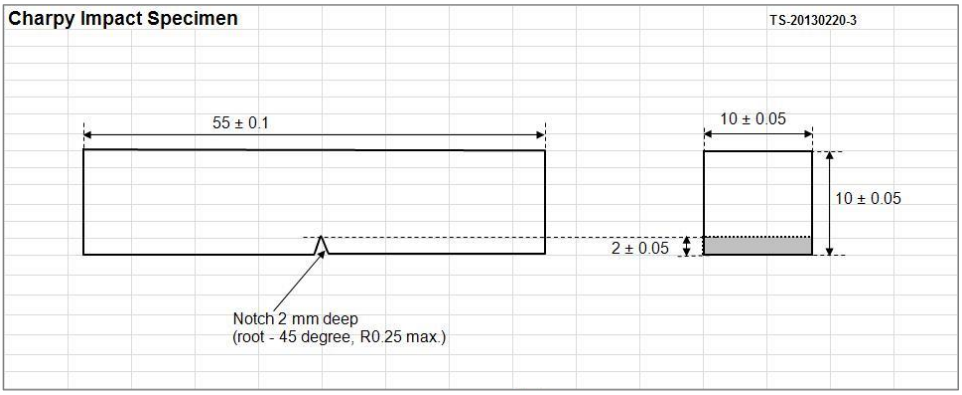

Figure 6. Standard Charpy impact specimen

3.3 Static fracture testing

3.3.1. Preparation of fracture specimens

The fracture specimen design selected for this research was a single-edged bend bar (SEB) specimens with a dimension of 10×10×50 mm^3 with a 3.5 mm deep notch and with a 1.5 mm deep side groove at each side. Such deep (15%) side grooves were employed to maintain crack tip constraint, which can be easily lost in ductile materials. In both precracking and static fracture testing the bar specimens were loaded in three point bending (TPB) mode.

Prior to the static fracture (J-R) testing [13], the SEB specimens were fatigue-precracked to roughly 5 mm depth at room temperature in air: the fatigue loading was stopped at a crack length-to-width ratio near 0.5. A typical condition for starting crack growth was a cyclic load of 600±400 N at 20 Hz, and this cyclic load was decreased to ~40% in the end of fatigue loading. The numbers of cycles taken for ~1.5 mm growth were in the range of 70k–200k for the majority

of specimens. For all specimens tested, the average initial crack length of the precracked specimens was 5.1 mm with a standard deviation of 0.22 mm.

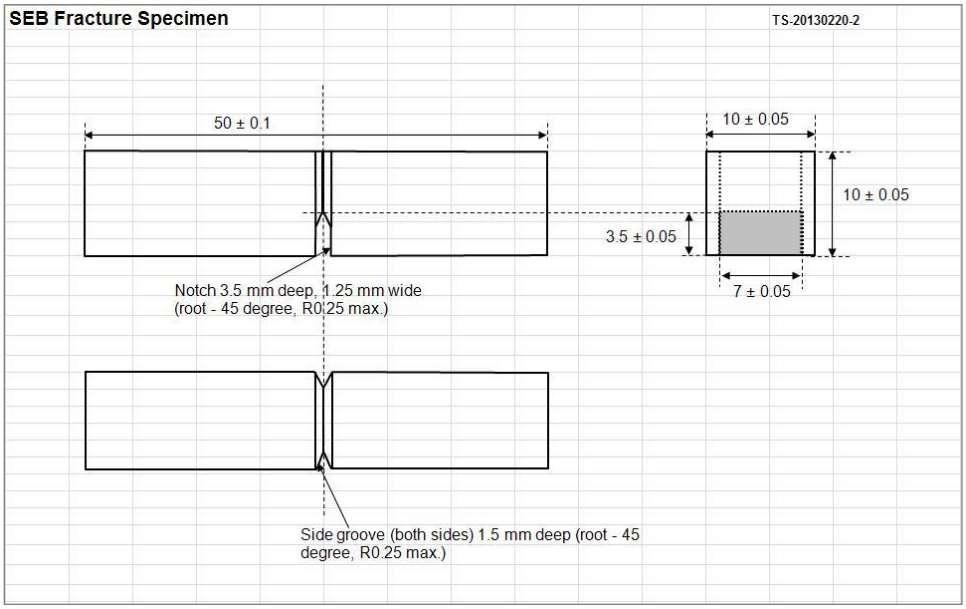

Figure 7. Single-edged bend bar (SEB) specimen for static fracture resistance (J-R) testing

3.3.2. Simplified data acquisition

Simplification in data acquisition was pursued based on the consideration that the displacement measurement using attached gage was not needed as we chose to use the normalization curve method. Further, a modified curve normalization to accommodate the simplified displacement reading has been developed for miniaturized testing in high radiation area and in controlled environment [14-16]. This new J-R analysis procedure was further developed for application to the present SEB specimens and described in the next section.

A technical justification for the removal of attached displacement gage is given below. In typical static fracture testing a precision displacement gage, such as Wheatstone bridge type clip gage or linear variable differential transducer (LVDT), is usually attached to the fracture specimen to measure the crack-mouth displacement or the axial deflection, depending specimen type. In the J-R curve calculation following the test standard [13], the J-integral is divided into two components of elastic and plastic energies. It can be easily recognized that the elastic J component is a well-defined function of load, crack length, and elastic constants [13], none of which requires displacement measurement. A precise measurement of elastic displacement or load/displacement slope is required only if crack growth is monitored by unloading compliance method. The plastic J component indeed requires displacement data but plastic component only. Detailed practices in J-evaluation indicate that the elastic component of measured displacement is not used in any methods of J-R curve calculation except for compliance data in the unloading compliance method. In the normalized curve method, in particular, the plastic displacement at each point can be easily separated from the total displacement using the initial slope of load-displacement curve and updated compliance value, which is calculated as a function of crack

length. To guarantee the accuracy of plastic displacement data, however, it is important to take a correct procedure that can effectively separate the plastic displacement component from the total displacement measured. It is well understood that the total displacement data obtained from a built-in displacement measuring device include the displacement components of all parts and contacts in the whole load train, and therefore, are usually not accurate enough to be directly used in the unloading compliance method, where an accurate measurement of elastic unloading slopes is essential for converting those to crack length data. In the curve normalization method, however, any non-plastic components of total displacement can be easily removed in the J-R curve calculation procedure. In this work, therefore, the major simplification made in the testing setup was removing the external displacement gage.

3.3.3. Static fracture testing

Fracture resistance (J-R) tests were carried out in a quasi-static TPB mode for the SEB specimens in the same MTS servo-hydraulic testing machines used for tensile testing. The test temperatures for the static J-R tests ranged from -175 °C to 400 °C. As in the tensile testing, all tests were carried in air and temperature control was by either infrared light heating or liquid nitrogen cooling. All tests were carried out in a displacement-controlled three-point bending mode at a crosshead speed of 0.005 mm/s with a temperature control within $\pm 2^{o}$C. Each specimen was soaked at the target temperature for 5–10 minutes prior to the J-R testing. Both fracture testing and evaluation were performed following the standard procedure in the ASTM Standard E1820 [13] and the modified analysis procedure [16].

To use the curve normalization method, two datasets are needed for input: a load-displacement curve, up to ~50% of the maximum load if passing the maximum load, and the initial and final crack lengths. The load versus load-line displacement data were recorded at a data acquisition rate of 2 per second, and used for the analysis to obtain J-R curve and interim fracture toughness (J_Q). After each J-R test, the unbroken specimen was fatigue-loaded in air to make a mark for the final crack length before the final separation. The initial and final crack lengths were then measured using an optical measure scope.

3.4 Analysis of fracture test data

This section describes the procedure to convert a dataset of load-displacement data and initial and final crack lengths to a J-integral versus crack growth (Δa) curve and then to determine fracture toughness. The steps and equations described here can be considered to follow the standard test method unless specified otherwise. Modifications were made in a few places to accommodate the simplification in the data acquisition: the main modification made in J-R data calculation is the process regarding the use of the displacement data either from the built-in displacement device or from cross-head movement.

3.4.1. Calculation of load-'plastic' displacement data

Since no external displacement gage was attached to the SEB specimens during testing, the displacement data recorded contains undesirable components from the flexibility of whole load train including specimen-jig contacts. Using the plastic component only is considered the

best way to avoid incurring additional errors, and therefore, the first step of the calculation procedure is to produce a load-plastic displacement ($P_{(i)} - v_{p(i)}$) data from the recorded load-total displacement data ($P_{(i)}$ *vs.* $v_{(i)}$). For each data point (i), the plastic displacement component is extracted from the total displacement by using load-line compliance ($C_{LL(i)}$) and a constant C_A [16]:

$$v_{p(i)} = v_{(i)} - (C_{LL(i)} + C_A)P_{(i)} = v_{(i)} - C^e_{LL(i)}P_{(i)}. \qquad (1)$$

The initial (composite) load-line compliance, $C_{LL(0)}+C_A$, is measured from the linear portion of experimental load-displacement curve and the constant C_A, the compliance from load train except specimen itself, is determined as $C_{LL(0)}$ can be calculated from the measured initial crack length. The plastic displacement is set to zero at the first point and calculated to be zero in the whole linear elastic loading region. Once the constant C_A is determined, the plastic displacements for the next points can be progressively calculated using the effective compliance $C^e_{LL(i)}$. At each point the $C_{LL(i)}$ value is updated by using the following equation given as a function of crack length ($a_{(i)}$) [13]:

$$C_{LL(i)} = \frac{1}{EB_e}\left(\frac{S}{W-a_{(i)}}\right)^2\left[1.193 - 1.98\left(\frac{a_{(i)}}{W}\right) + 4.478\left(\frac{a_{(i)}}{W}\right)^2 - 4.443\left(\frac{a_{(i)}}{W}\right)^3 + 1.739\left(\frac{a_{(i)}}{W}\right)^4\right], \quad (2)$$

where E is the elastic modulus (180 to 200 GPa at 400 to -175 ℃), ν the Poisson ratio (=0.28), B_e the effective thickness (=9.1 mm), S the span of load supports (= 50 mm), and W the width of specimen (10 mm). The crack length and compliance are updated for each point as the curve normalization calculation progressively provides the values of J-integral and crack length.

3.4.2. Calculation of J-integral

The present curve normalization method and traditional unloading compliance method use different techniques for evaluation of crack lengths, common equations are used in the calculation of *J*-integral and stress intensity factor *K* [13]. Those equations are summarized as below since many of them are intermingled in the application of normalization method. The total J-integral at point (i) is defined as the sum of elastic and plastic components ($J_{e(i)}$ and $J_{p(i)}$):

$$J_{(i)} = J_{e(i)} + J_{p(i)} = \frac{K^2_{(i)}(1-\nu^2)}{E} + J_{p(i)}, \qquad (3)$$

where $K_{(i)}$ the stress intensity factor or linear-elastic component of fracture toughness. When all load-displacement and geometrical parameters are known, the plastic component $J_{p(i)}$ can be calculated by

$$J_{p(i)} = \frac{1.9A_{p(i)}}{B_N(W-a_{(i)})}, \qquad (4)$$

where the $A_{p(i)}$ is the plastic energy applied to the specimens or area below load-plastic displacement curve, B_N the net specimen thickness with side grooves (=*7 mm, with B* =10 mm). In practical calculation, a discretized equation is used [13]:

$$J_{p(i)} = \left[J_{p(i-1)} + \left(\frac{1.9}{b_{i-1}}\right)\left(\frac{A_{p(i)}-A_{p(i-1)}}{B_N}\right)\right]\left[1 - 0.9\,\frac{a_{(i)}-a_{(i-1)}}{b_{(i-1)}}\right], \qquad (5)$$

where $a_{(i)}$ and $b_{(i)}$ are the crack length and uncracked ligament at point (i), respectively, and

$$A_{p(i)} - A_{p(i-1)} = \frac{[P_{(i)}+P_{(i-1)}][v_{p(i)}-v_{p(i-1)}]}{2}. \qquad (6)$$

The stress intensity factor $K_{(i)}$ is given as a function of load P and geometrical parameters only [13]:

$$K_{(i)} = \frac{P_{(i)}S}{(BB_N)^{\frac{1}{2}}(W)^{\frac{3}{2}}} \frac{3(a_{(i)}/W)^{\frac{1}{2}}\left\{1.99-(a_{(i)}/W)(1-(a_{(i)}/W)\left[2.15-3.93(a_{(i)}/W)+2.7(a_{(i)}/W)^2\right]\right\}}{2(1+a_{(i)}/W)(1-a_{(i)}/W)^{\frac{3}{2}}}. \qquad (7)$$

3.4.3. Calculation of normalized load-displacement data

The first section of a load-displacement curve before reaching maximum load corresponds to the crack blunting regime or the initial section of a J-R curve with a steep theoretical slope of $2\sigma_Y$. This flow stress σ_Y is defined as the average of yield stress and ultimate tensile stress measured at the fracture test temperature. As described in the ASTM standard, the normalized load and displacement ($P_{N(i)}$, $v'_{p(i)}$) are defined as generalized parameters that are insensitive to, if not independent of, the geometry of test specimen and given in stress and strain units, respectively. The normalized load and displacement up to, but not including the maximum load is calculated by [13]:

$$P_{N(i)} = \frac{P_{(i)}}{\mathrm{WB}\left[\frac{W-a_{(i)}}{W}\right]^2}, \qquad (8)$$

$$v'_{p(i)} = \frac{v_{p(i)}}{\mathrm{W}} = \frac{v_{(i)}-C^e_{LL(i)}P_{(i)}}{\mathrm{W}}. \qquad (9)$$

Here, the crack length $a_{(i)}$ is calculated by:

$$a_{(i)} = a_0 + \frac{J_{(i)}}{2\sigma_Y}. \qquad (10)$$

As can be quickly realized in practical calculation, the evaluation of these equations requires to solve circular references among parameters: in the above equations, for example, the $a_{(i)}$ needs to be evaluated first to calculate others such as $C^e_{LL(i)}$ (or $C_{LL(i)}$), and then $P_{N(i)}$. In this work a simple technique that uses the (i-1)-th value for the i-th point calculation was adopted as the data acquisition interval is very small (< 0.05 mm). Any error incurred by this simple technique is easily compensated by iteration to match the calculated final crack length with the measured value.

The next step is calculation of normalized load-displacement data for the post-maximum load positions. Since the crack blunting line (Eq. 10) cannot be used for these points, an approximation using a proper function is needed for this portion which represents the major crack growth to final failure or test stop. A line should be drawn from the final normalized load-displacement pair tangent to the curve around the maximum load point. The connection with a simple linear line could provide highly accurate outcome for the J-R curve in most cases although in the standard method a normalization function with four fitting coefficients is recommended. A similar non-linear function described by four constants was suggested and has been used for high strength steels [16]:

$$P_{N(i)} = \frac{P_{N(m)} + x\left[v'_{p(i)} - v'_{p(m)}\right]}{1 + y\left[v'_{p(i)} - v'_{p(m)}\right]^2}, \qquad (11)$$

where the point denoted by the subscript '*m*' is the maximum load point, and the variables *x* and *y* are changed until the best fit curve is reached. Two criteria used for searching the best fitting function are (a) if the functional continuity between the fitting function and the calculated data using the blunting line ($J=2\sigma_Y \Delta a$) is achieved around the maximum load point and (b) if the normalized load at final data point given by the fitting function matches the value calculated from the measured final crack length. Once the iteration searching for satisfying these criteria is completed, the whole J-R curve is easily constructed.

3.4.4. Construction of J-R curve and determination of fracture toughness

As the full normalized load versus displacement is established, the crack extension beyond the crack blunting regime can be calculated by an inverse function of Eq. (8):

$$a_{(i)} = W\left\{1 - \left[\left(\frac{P_{(i)}}{P_{N(i)}}\right)\left(\frac{1}{WB}\right)\right]^{1/2}\right\}. \qquad (12)$$

In the process of calculating crack lengths using normalization, the *J-R* curve, i.e., *J-Δa* data is simultaneously obtained at each data point since the crack extension amount *Δa* is simply given by $a_{(i)} - a_0$.

As the final step of fracture testing and evaluation, fracture toughness was determined on each J-R curve following the ASTM standard method E1820 [13]. The interim fracture toughness values (J_Q) were determined at the intersection of the constructed J-R curves and the 0.2 mm offset line of the blunting line ($=2\sigma_Y \Delta a$). The final fracture toughness data were given in the form of stress intensity factor, K_{JQ}, which can be converted from the J_Q data using the following relationship:

$$K_{JQ} = \sqrt{(J_Q \cdot E)/(1-\nu^2)}. \qquad (13)$$

4. RESULTS OF MECHANICAL TESTING AND EVALUATION

4.1 Tensile strength and ductility

Figure 8 displays the temperature dependences of yield strength (YS) and ultimate tensile strength (UTS). Overall, both the YS and the UTS decreased with test temperature. Since these cast alloys commonly experienced strong strain hardening on testing, the difference between YS and UTS was large, about 200 MPa or larger. The temperature dependence shows, however, that those strength parameters behave differently, depending on temperature region: the YS decreases gradually with temperature over the whole test temperature, while the UTS shows a large drop between -100 °C and room temperature and then decreases gradually at similar rate to YS. Further, the alloys CF8 and CF8M have lower YS when compared to the other two alloys CF3 and CF3M. However, the cause for such variation is not known at the moment for the limited microscopy data; neither the chemical composition nor the ferrite volume fraction can consistently explain such relative strength behaviors among the model alloys.

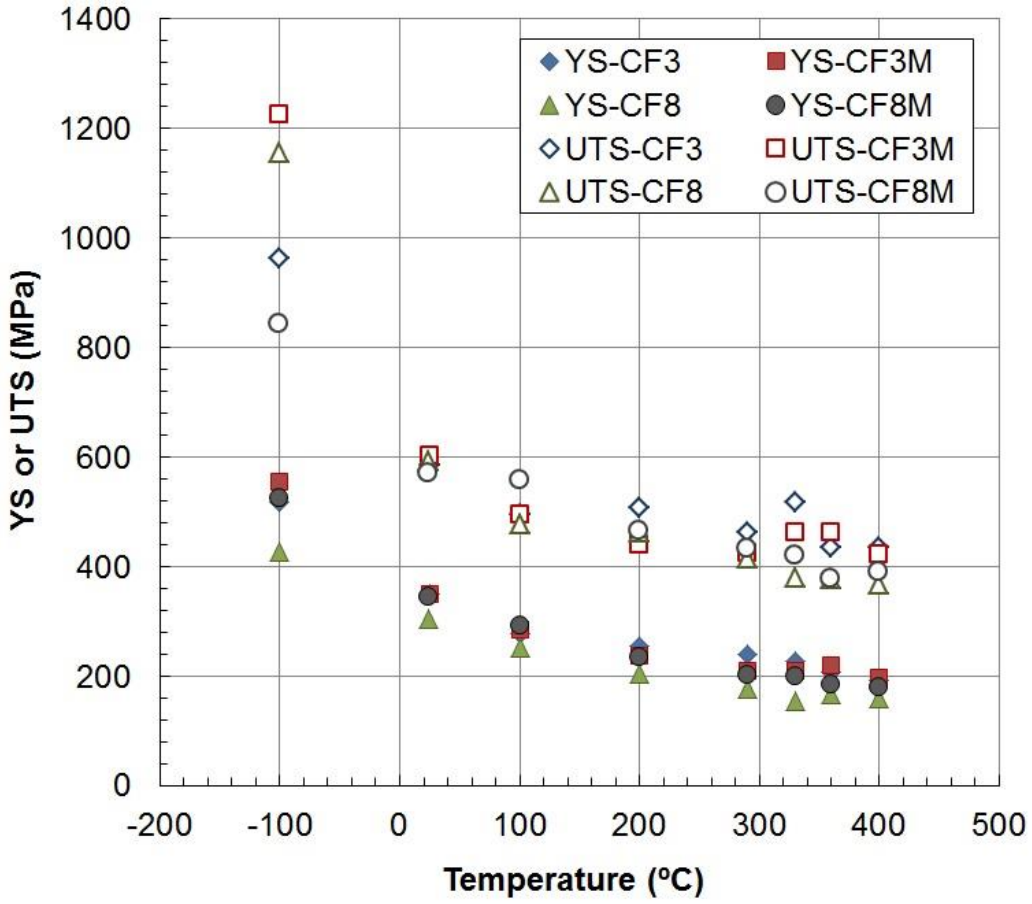

Figure 8. Temperature dependence of yield and ultimate tensile strengths in cast stainless steels.

It is impressive that the UTS values of CF8 and CF3M at -100 °C can reach well above 1 GPa and those of all alloys are in the range of 840–1230 MPa. At this temperature, the difference between YS and UTS reached ~730 MPa in CF8 alloy and ~670 MPa in CF3M alloy, while the smallest difference, found in CF8M alloy, was still more than 310 MPa. The work hardening amount, UTS-YS, at or above room temperature are consistently high, and such high hardening stresses should be because of the characteristic linear slip at low temperatures, which typically are found in low stacking fault energy (SFE) materials [17-20]. A single mechanism of highly linear but ordinary dislocation glide should be responsible for the consistent hardening at or above room temperature. At -100 °C, however, additional deformation mechanisms such as twinning and martensite formation are believed to be responsible for extra high work hardening in CF8 and CF3M alloys.

Figure 9 indicates a general trend that the ductility of model cast stainless steels decreases with test temperature. In detail, the rate of decrease is high up to 200 °C, from which the elongations become stagnant. Since these alloys retain high uniform ductility > 29% over the whole test temperature range, the necking ductility in engineering term, TE-UE, is only about 6% in average. Further, the CF8 and CF3M alloys, which showed the highest work hardening

amounts, have apparent minima both in UE and in TE at 200 °C and 360 °C, respectively. These ductility minima might be related to the interaction between solute atoms and highly linear dislocation slips. At -100 °C the CF3 alloy showed the highest ductility among the model alloys: both the UE and the TE are above 100%. This ultrahigh ductility should be due to a gradual formation of martensite particles and twins, which often maintains or increases work hardening rate at high strains [21].

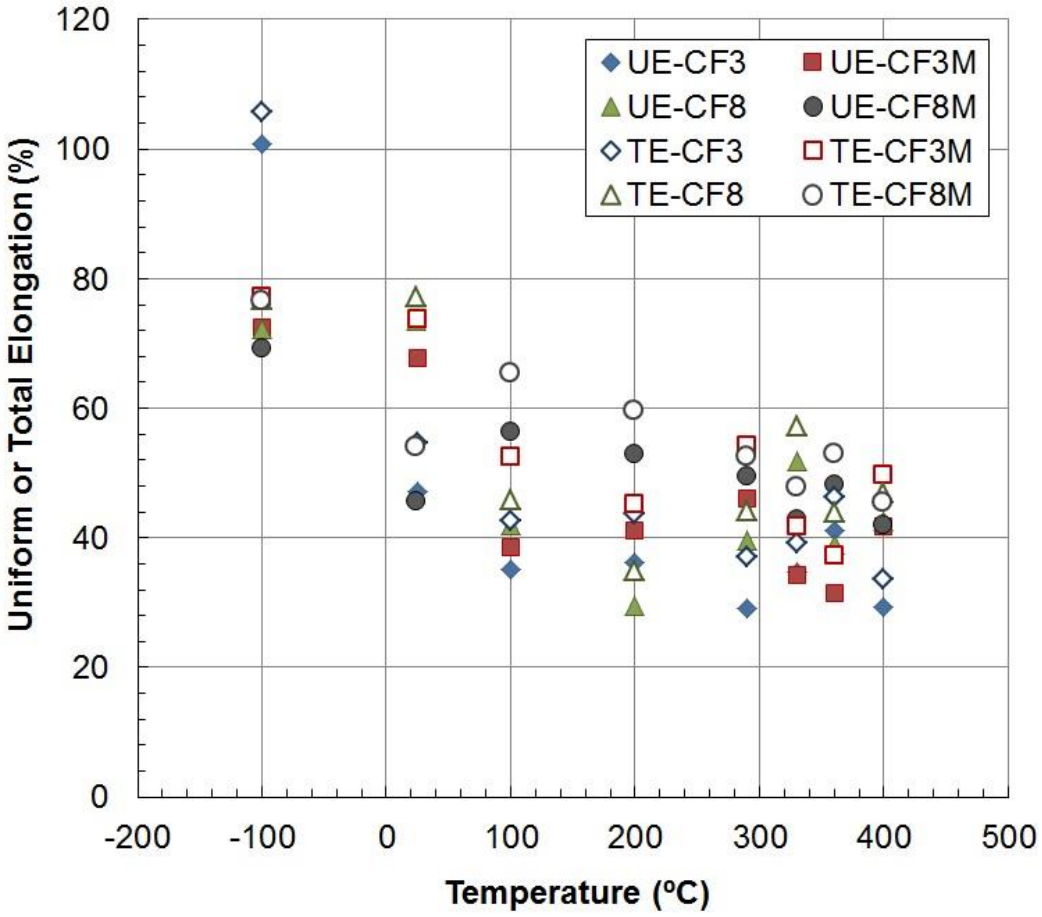

Figure 9. Temperature dependence of uniform and total elongations in cast stainless steels.

As well known, the extraordinarily high ductility and work hardening of these alloys originate primarily from their linear dislocation glide, which can generate higher internal stress and resulting strain hardening rate compared to the random dislocation glide [21]. This deformation mechanism can explain the temperature dependence of tensile properties: a characteristic behavior observed in the austenite dominant materials only is that both ductility and strength decrease with test temperature. Such simultaneous decrease of strength and ductility can be explained by the fact that the degree of linearity in slip band formation should decrease with temperature as the cross slip can more easily occur at higher temperatures.

Further, the ferrite phase might not directly contribute to ductility as much as the austenite phase; however, those should induce some particle hardening effect which contributes

to overall ductility. In a duplex microstructure, the harder phase (ferrite) usually deforms later than the softer phase (austenite), and the inhomogeneous distribution of stress between these two phases usually helps retain high work hardening rate.

It is also worth noting that over the whole aging temperature region (290-400ºC), both strength and ductility are not much temperature dependent. First, this indicates that the same deformation mechanism may be responsible for the plasticity in the temperature region. Having the same slip mechanism may help us compare the aging effects among alloys because we can avoid other complexities from involving different deformation mechanisms. Second, this temperature-insensitive behavior may indicate that there is little difference in the diffusion regime of light elements such as C and N in the aging temperature range. As we are to investigate the difference of aging effects focusing on the precipitation and phase stability behaviors, such consistent diffusion mechanism may cause little change in the aging mechanism over the aging temperature range. This hypothesis, if it is proven, should be able to provide a justification for the accelerated aging experiments.

4.2 Transition behavior of Charpy impact energy

Charpy impact energies were obtained from the standard sized specimens of four model alloys. Their temperature transition behaviors are compared in Fig. 10. The impact energy of model alloys showed clear but wide transition regions over the test temperature range of -196 to 100 ºC. Because of the high strength and ductility at low temperatures shown in precious section, however, lower shelf or brittle fracture was not observed up to the liquid nitrogen temperature. The upper shelf was observed in the 0–100 ºC region for CF3, CF8, and CF8M, but not for CF3M, which showed excessive plasticity at 100 ºC (a 'no test' case). The upper shelf energy for CF3 appears to be about 180 J, but is the only one below 200 J.

The ductile-brittle transition temperature (DBTT) of absorbed energy is usually defined as the temperature corresponding to the average of lower and upper shelf energies [12]. As the lower shelf could not be defined, the DBTT could not be determined, either, for all of the model alloys. Instead, a transition temperature parameter, T_{100J}, was defined here to compare materials: the T_{100J} values were determined for the model alloys. The T_{100J} values, which correspond to the temperature to have an impact energy of 100 J, were determined to be -125, -143, -118, and -175 ºC for CF3, CF3M, CF8, and CF8M, respectively. It was noticed that the lowest T_{100J} was measured from the CF8M alloy, which showed overall the highest value combination of strength and ductility.

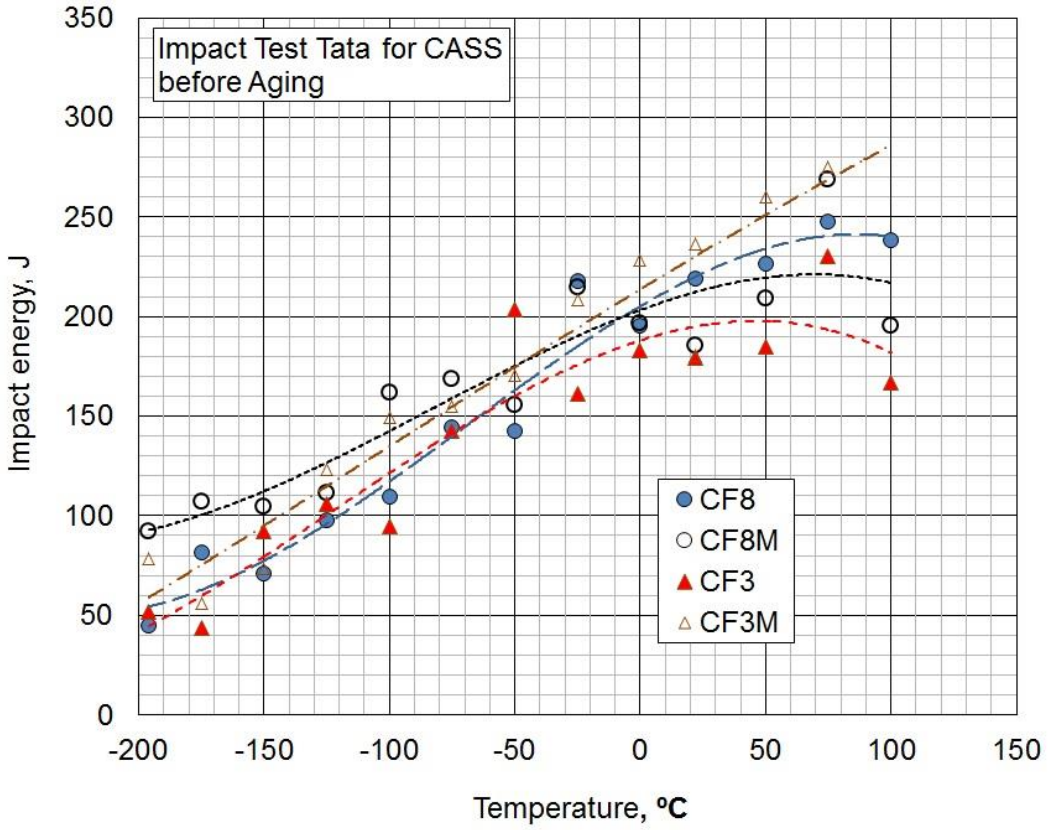

Figure 10. Ductile-brittle transition behavior of impact energy in the cast stainless steels. No lower shelf was observed.

4.3 Static fracture behavior and its temperature dependence

Figures 11 – 14 display the static fracture resistance (*J-R or J-Δa*) curves of pristine cast stainless steels, which were generated from the load-load line displacement curves and crack length measurements using the modified normalization method described above. These figures indicate that the cast stainless steels have commonly high fracture resistance (*J-R*) and high slope (*dJ/da*) over the test temperature range: in all cases the J-value increase passing 200 kN/m at a small Δa of 0.5 mm and the slopes at Δa ≈ 0.5 mm are well above 100 MN/m^2. Along with the overall high fracture toughness, demonstrating high slope or tearing modulus, *dJ/(Eda)*,is of importance for structural integrity since it is a measure of crack arresting power and stable crack growth.

Figure 11 indicates that the fracture resistance tends to be relatively lower at the elevated temperatures (≥ 200 ºC) than at lower temperatures (≤ RT). This can be explained by the temperature dependence of tensile properties since the product of the strength and ductility is generally proportional to fracture toughness in ductile fracture. This trend, however, is not always consistent as seen in Fig.13 for the CF8 alloy, where the J-R curve for -175 ºC is at the lowest position among the curves.

Although Figures 11 – 14 can confirm that the model alloys before aging have fairly high fracture resistance at all test temperatures, it needs to be considered that the SEB specimen size ($10\times10\times50$ mm^3) is within the category of subsize specimens for the extraordinary ductility of the duplex alloys. Two general characteristics regarding the subsize specimen test and analysis technique are considered to help correct interpretation of the results: First, the small maximum crack growths of about 2.5 mm or less could be obtained from the 10 mm wide specimens because the nominal initial uncracked ligament was limited to about 5 mm. Such small crack growths and corresponding short J-R curves might result in steeper slopes. Second, as always observed in an indirect crack measurement method, the normalization method uses an artificial linear line ($J=2\sigma_Y\Delta a$) for crack blunting regime [13] and thus the transition to the J-R curve portion in the crack growth regime could be not continuous. A continuous transition is usually closer to the natural phenomenon. Thanks to the consistently high ductility, the transition was always smooth and continuous in this research.

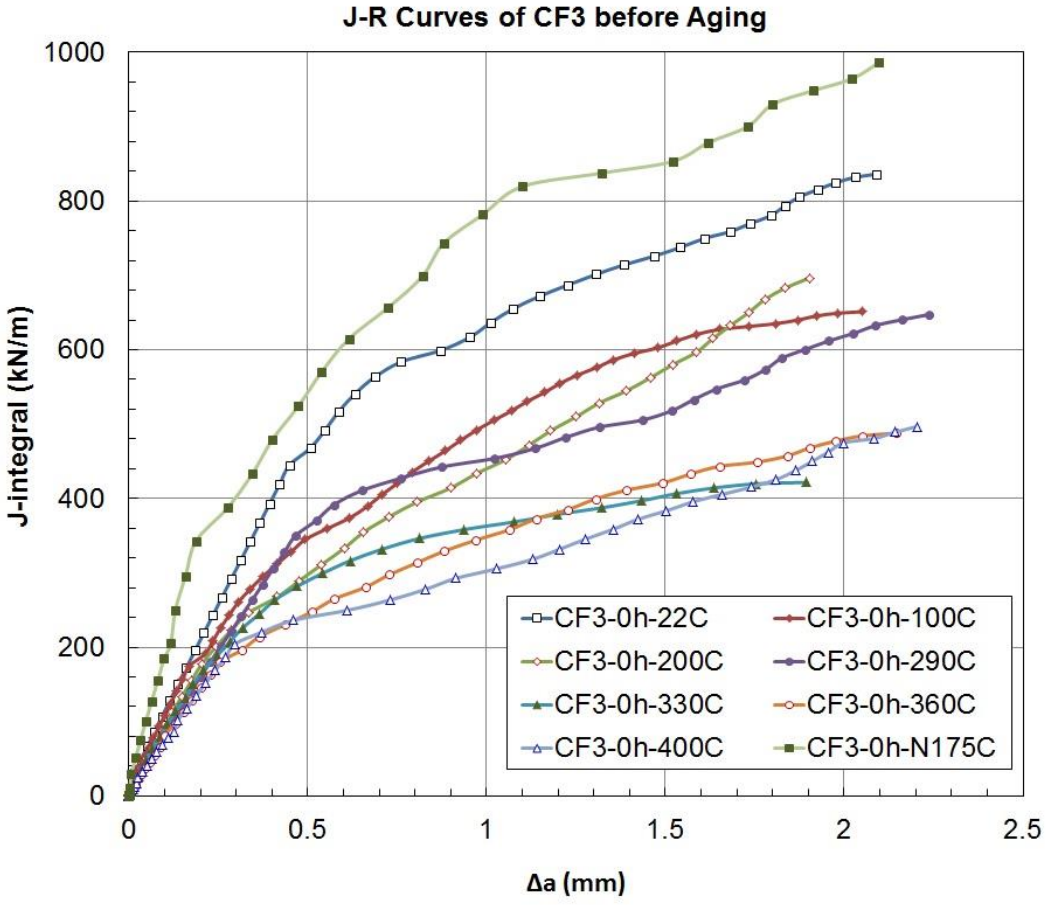

Figure 11. Fracture resistance (J-R) curves for the CF3 alloy, which were generated from load-load line displacement curve and crack length measurements using curve normalization method.

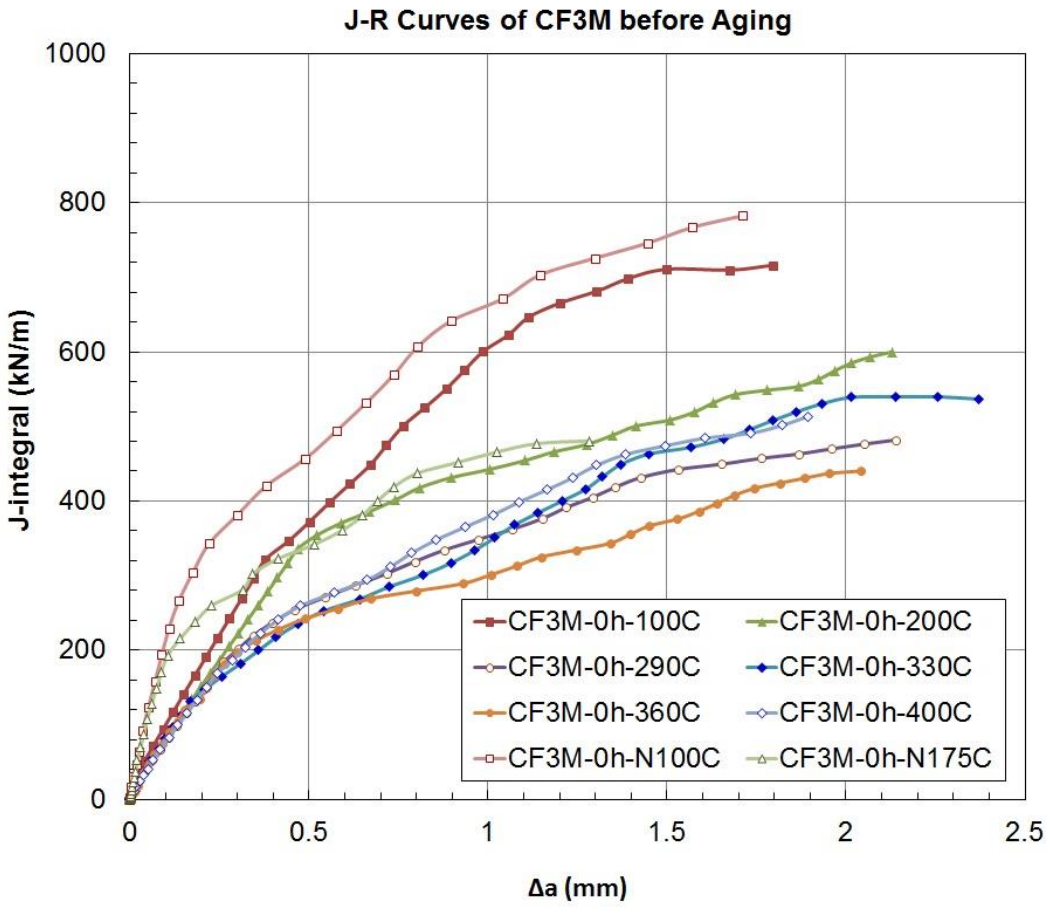

Figure 12. Fracture resistance (J-R) curves for the CF3M alloy, which were generated from load-load line displacement curve and crack length measurements using curve normalization method.

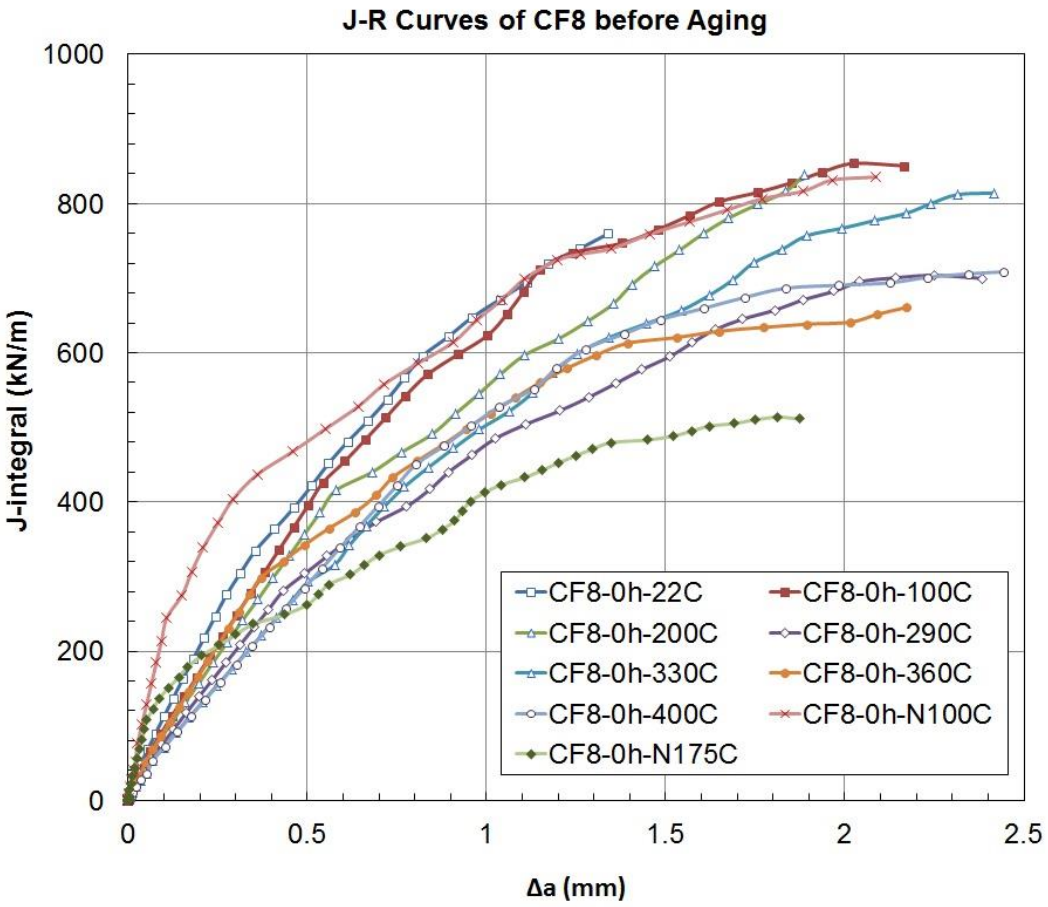

Figure 13. Fracture resistance (J-R) curves for the CF8 alloy, which were generated from load-load line displacement curve and crack length measurements using curve normalization method.

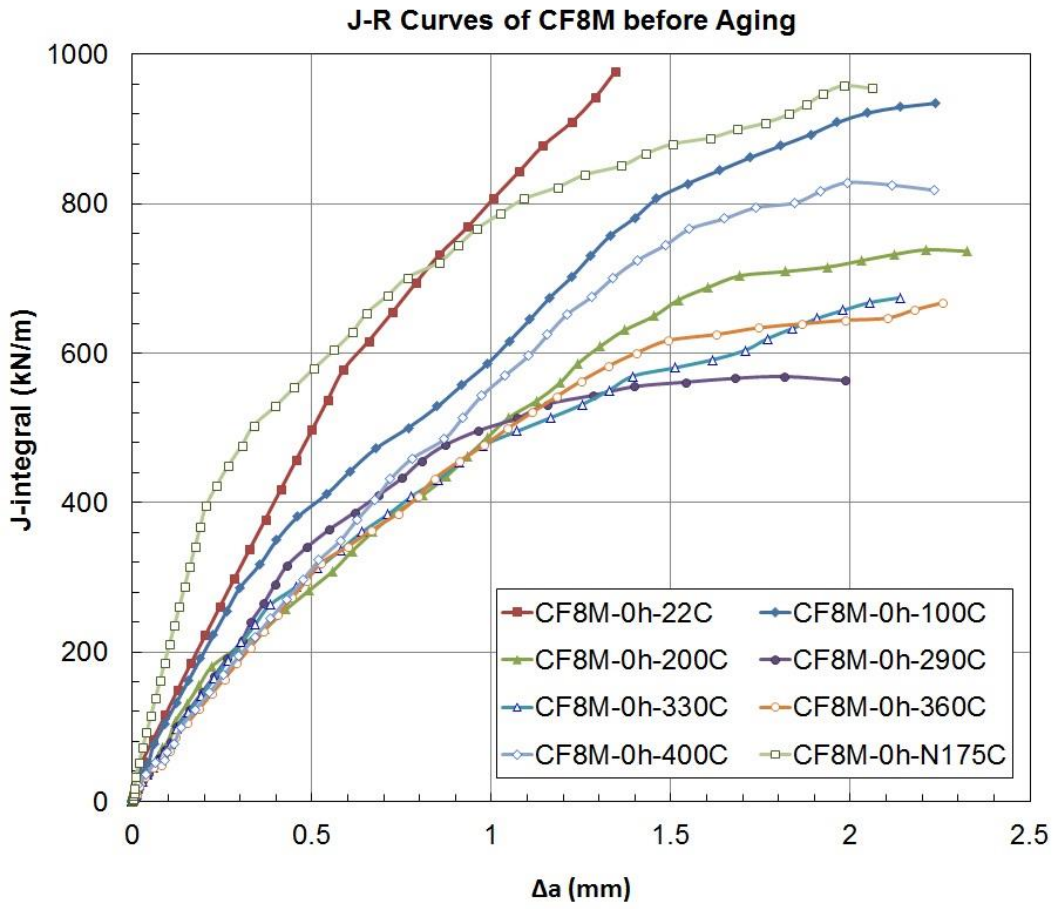

Figure 14. Fracture resistance (J-R) curves for the CF8M alloy, which were generated from load-load line displacement curve and crack length measurements using curve normalization method.

On the J-R curves displayed above the interim fracture toughness or the critical J-integral (J_Q) for each test was determined at the intersection of the J-R curves and the 0.2 mm offset line or the straight crack blunting line. Then, J_Q value was converted to K_{JQ} value using Equation (13). Note that the fracture toughness values remain as interim values as a large portion of the fracture toughness data obtained for the model case stainless steels are too high to be validated for plain strain conditions.

Figure 15 displays the temperature dependence of fracture toughness (K_{JQ}) for all four model alloys. The plots indicate that no alloy demonstrates outstandingly high or low fracture toughness at a temperature or consistently higher fracture toughness in the test temperature range. Further, all of the four cast stainless steels before aging were proven to be high toughness materials as no fracture toughness below 200 MPa$\sqrt{m}$ was measured from the model CASS materials, and naturally some specimens experienced excessive plasticity in testing.

It was also found that a peak in fracture toughness was measured for each alloy at -100 to 100 ºC, below which K_{JQ} decreased with decreasing temperature. This decrease is believed to be

the ductile to brittle transition (DBT), but no fracture test has shown brittle mode or reached the lower shelf within the test temperature range. Above the peak, the fracture toughness K_{JQ} tends to decrease with temperature up to 360 °C or 400 °C. Similarly to the temperature dependences of strength and ductility, the variation of fracture toughness in the aging temperature region (290–400 °C) was limited although two materials groups (CF3 and CF3M versus CF8 and CF8M) showed clear divergence in the higher temperature region of 330–400 °C.

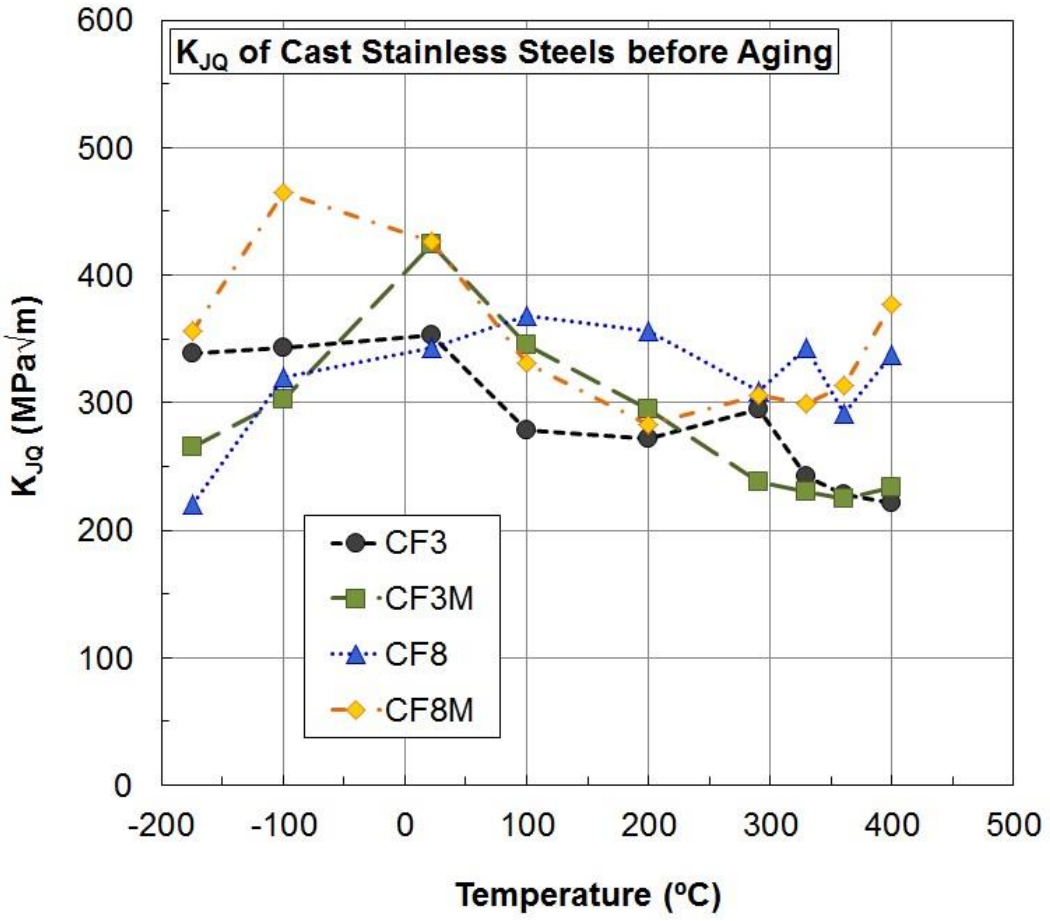

Figure 15. Fracture toughness (K_{JQ}) as a function of test temperature. Note that the critical J-integral (J_Q) was determined first on each J-R curve and then converted to K_{JQ} using Equation (13).

5. COMPUTATIONAL STUDY ON PRECIPITATE PHASES

5.1. Calculation method and conditions

A preliminary computational study on long-term thermal aging phenomena was performed to predict precipitation behavior during ageing treatments and eventually to accurately

interpret experimental results and understand aging degradation mechanisms. This preliminary calculation was focused to simulate equilibrium precipitation behavior in the four model alloys (CF3, CF3M, CF8 and CF8M) using CALPHAD method [22] with the database and software options of OCTANT [23] and PANDAT [24]. No kinetics was involved in this calculation but the result will be used to refine future calculations focusing on the kinetics behaviors of precipitations on long-term aging.

All major alloy elements, Fr, Cr, Ni, Mo, and Si, and key trace elements, C and N, were taken into account in the calculation. For each alloy, two step calculations were conducted to obtain equilibrium data under assumption of thermodynamic equilibrium conditions. The first step was to generate data on phase fraction versus temperature from 1600 to 1200 °C. The result of this calculation was used to determine the austenite composition when specified amounts of ferrite (BCC) were formed during casting process. The amount of ferrite is provided by optical microscopy. The second step was to calculate precipitate phase fraction versus temperature in the temperature range of 250 – 500 °C for austenite using the composition from the first step.

5.2. Precipitation behaviors

Figures 16 – 19 display the results of calculation on equilibrium precipitates, where the mole fractions of phases are given as functions of aging temperature. In addition to the major phases, i.e., ferrite and austenite, multiple known phases were predicted to precipitate the dual phase structure in equilibrium condition. Those equilibrium precipitates are G-phase, chromium nitride (Cr_2N), Laves (η) phase, $M_{23}C_6$ carbide, π-phase, and σ-phase. Discussion below focuses on the temperature and materials dependences of precipitation of these phases.

Calculation results show that more G-phase can be formed at low temperature and the mole fraction decreases linearly with temperature. Its mole fraction was 3–7% at 250 °C and became close to zero at slightly above 350 or 400 °C, depending on alloys. It appears that the two alloys with relatively lower N content, CF3M and CF8, have formed higher amounts of G-Phase, while the lowest amount of G-phase was predicted for the CF8M alloy. The G-phase is an fcc intermetallic phase with a complex composition. Its precipitation usually occurs in the δ-ferrite and at the ferrite-austenite interfaces up to above about 350°C, particularly the formation of Ni, Si, Mo rich G-phase which can reach up to 12% by volume in Mo-containing CASS []. Carbon also is known to enhance G-phase precipitation. The G-phase does not appear to contribute significantly to hardening and loss of toughness.

The chromium nitride (Cr_2N) is commonly formed in high N stainless steels. It formed only above certain alloy-dependent temperature ranging from 270 to 330 °C, above which mole fraction was almost constant and always below 2% for the present model alloys.

Relatively large amounts (~4%) of Laves (η) phase were predicted to form in the CF3M and CF8M alloys containing high Mo contents (2.3 wt.%). Negligible amounts of η-phase are formed in the other two alloys. The graphs for the mole fraction of η-phase show that the η-precipitation depends slightly on aging temperature. The Laves (η) phase particles are hexagonal crystals that are composed of Fe_2Mo in many molybdenum-containing alloys. Laves phase is often found as small equiaxed particles intragranularly, and occasionally found on the grain boundaries [10,15]. Usually the Laves phases are considered detrimental to ductility and fracture toughness, while their effects on creep and high temperature deformation are not certain.

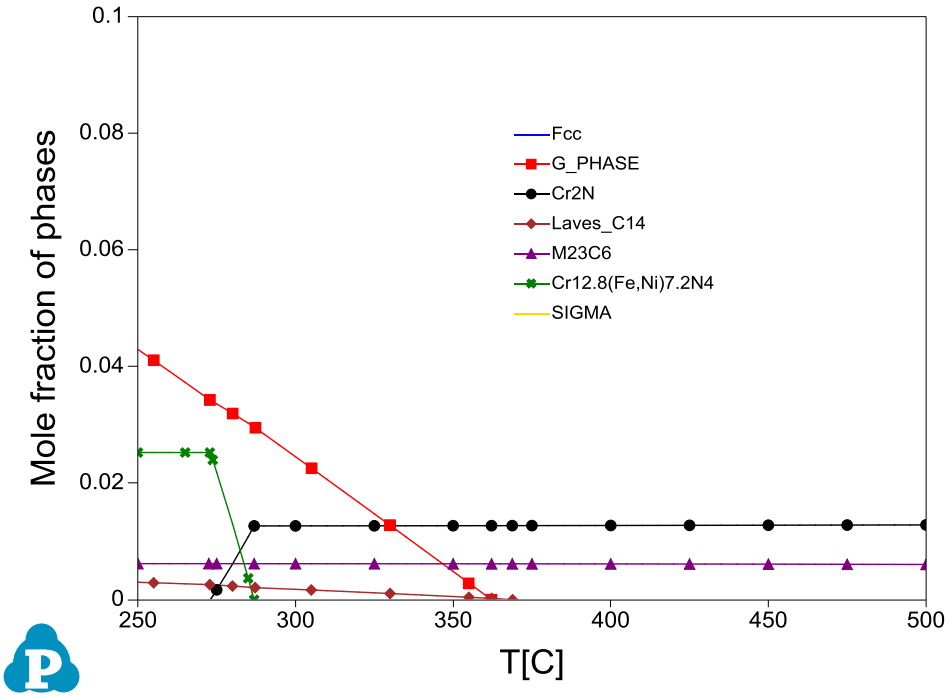

Figure 16. Precipitation behavior in CF3 (304L) with 7.7% ferrite.

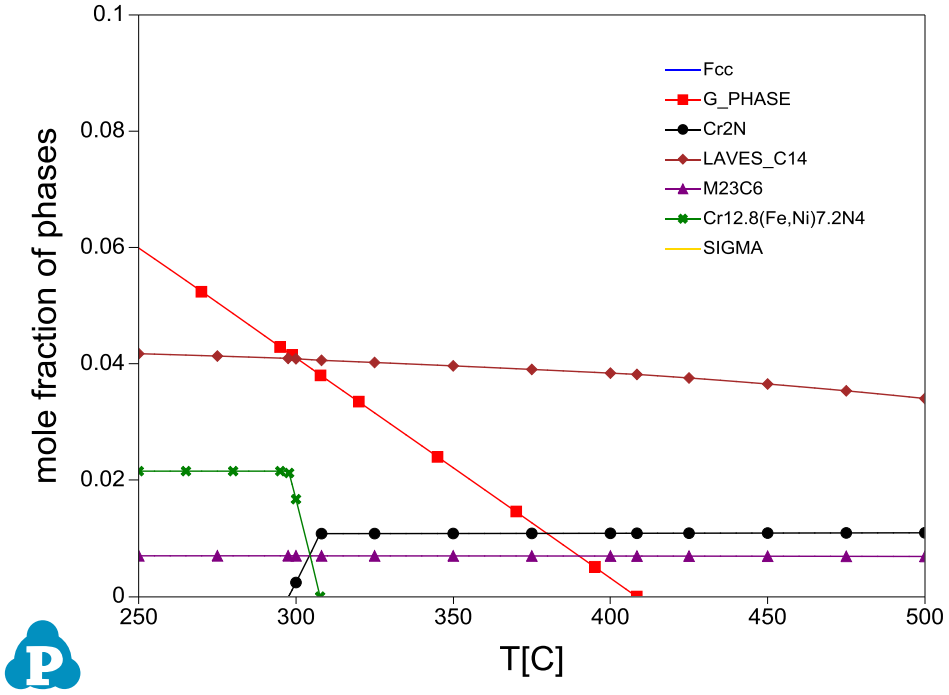

Figure 17. Precipitation behavior in CF3M (316L) with 11.5% ferrite.

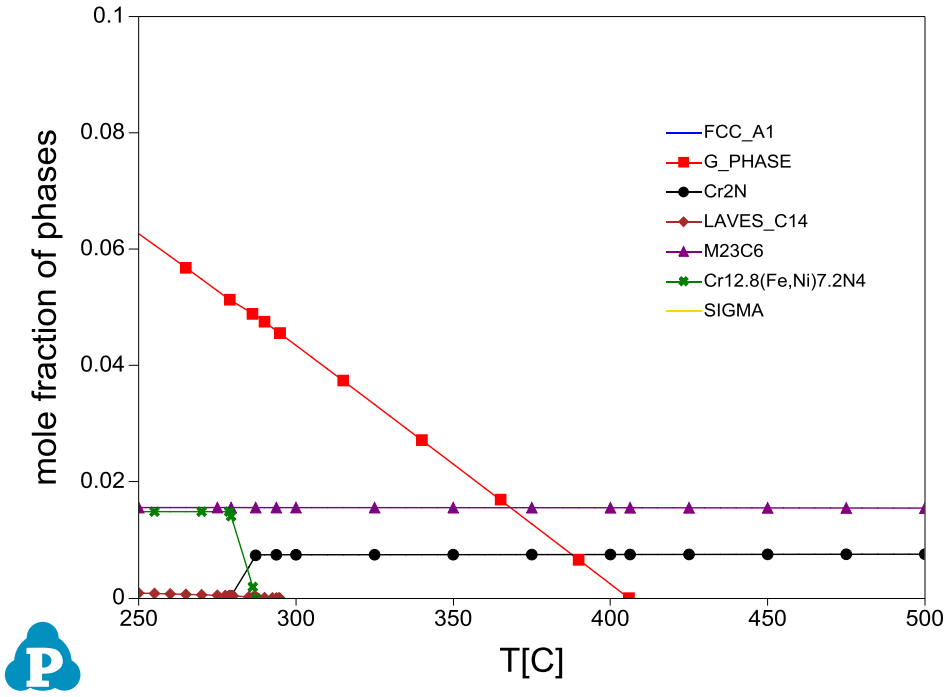

Figure 18. Precipitation behavior in CF8 (304) with 7% ferrite.

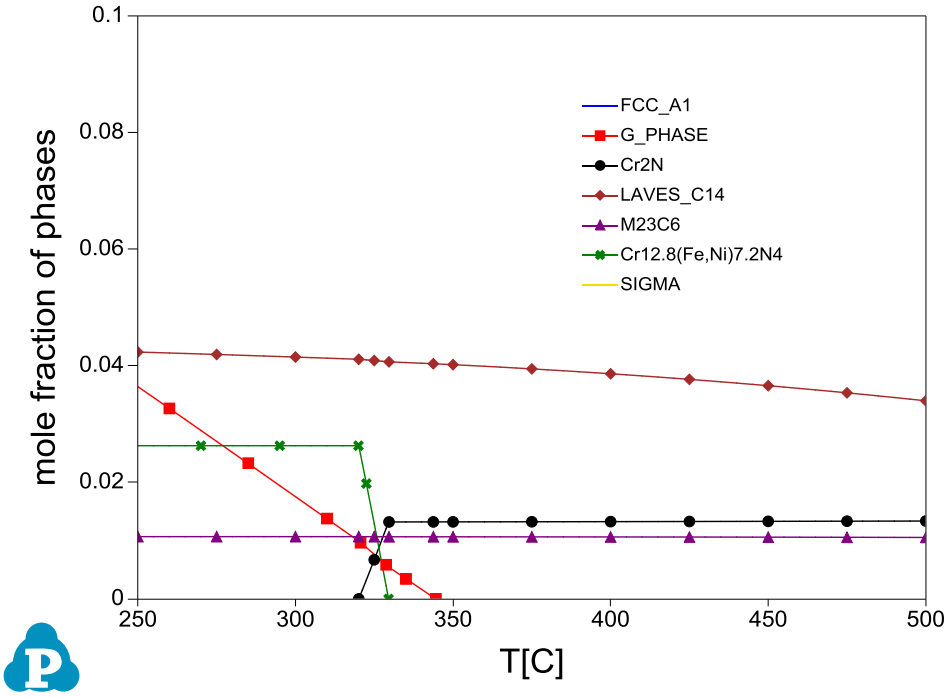

Figure 19. Precipitation behavior in CF8M (316) with 11% ferrite.

As in many steels, the most common high number density precipitate in CASS is the $M_{23}C_6$ carbide phase, where the metal atom (M) is most likely to be chromium [25,26]. Calculation result shows that this type carbide forms in all four model alloys and the mole fraction is almost temperature independent. The amount is mainly dependent on the C content. The lattice parameters of face-centered cubic $M_{23}C_6$ tend to increase with aging temperature and time, reflecting an increase of the molybdenum content of the carbide [27]. The $M_{23}C_6$ carbides tend to precipitate at grain boundaries, twin boundaries, and even intragranularly. It is also known that cold working causes the $M_{23}C_6$ precipitates to form at deformation bands and grain boundaries [25].

The π-phase is a complex nitride form, $Cr_{12.8}(Fe,Ni)_{7.2}N_4$. This form of nitride has been found to precipitate intragranularly in the ferrite phase of duplex stainless steel or in Mn-bearing austenitic stainless steel [26]. Figures 16 to 19 commonly indicate that the mole fraction of the π-phase is retained at more or less 2% up to about 300 °C and then the phase disappears at higher temperatures. No π-phase is predicted to be found at about 350 °C or higher.

This CALPHAD calculation predicted that a large amount of sigma (σ) phase (>20%) would be formed in equilibrium (not shown in the figures). Kinetics calculation has predicted, however, that the formation process is much slower than the other phases mentioned above [1]. In a definite time, therefore, the mole fraction of the phase will be very small. The sigma (σ) phase is a well-known intermetallic precipitate in Fe-Cr material systems that are often associated with embrittlement. Sigma phase is a tetragonal crystal composed of $(Cr,Mo)_x$ $(Ni,Fe)_y$ [28], forming always at high energy interfaces such as triple points, grain boundaries, twin boundaries, and intragranularly at oxide inclusions. There is some evidence that the σ phase precipitates only form on previous $M_{23}C_6$ sites or grow where $M_{23}C_6$ precipitates are dissolving [27].

Figure 20 summarizes the precipitation behavior of phases at the temperatures selected for aging experiment: 290, 330, 360, and 400 °C. Key findings discussed above are re-summarized here for directly relating to these aging temperatures: (a) The G-phase formation is strongly dependent on aging temperature and is relatively enhanced in the CF3M and CF8 alloys, probably due to relatively lower N content. (b) The Fe_2Mo (Laves) phase forms preferably in the high Mo alloys: CF3M and CF8M. The mole fraction seems to be strongly dependent on Mo content (2.3 and 2.33 wt.%, respectively, for the two alloys). (c) The π-phase formed in the alloys with high Mo contents at the lowest aging temperature (290 °) only. (d) The simple nitride (Cr_2N) and common carbide ($M_{23}C_6$) formed in all model alloys, with weak dependence on aging temperature.

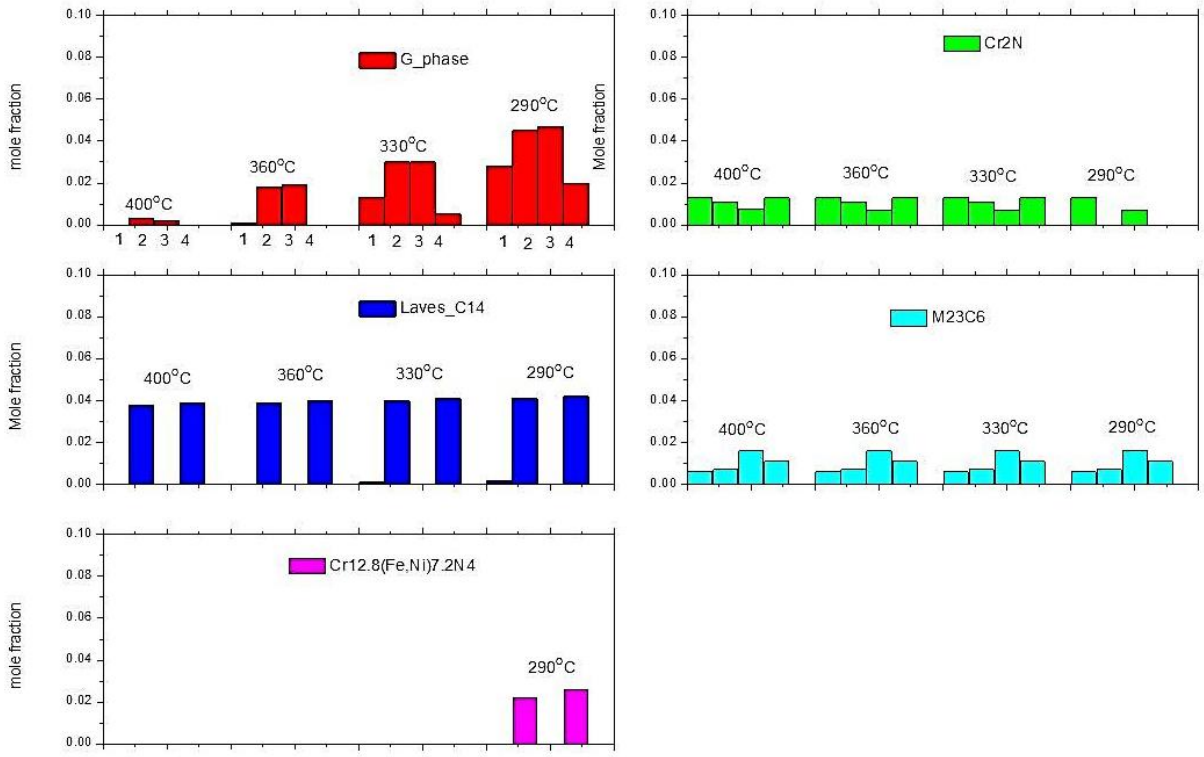

Figure 20. Summary of precipitate phases in equilibrium status. The numbers 1, 2, 3 and 4 denote CF3, Cf3M, CF8, and CF8M, respectively.

6. SUMMARY & CONCLUSION

Baseline materials evaluation has been carried out for model alloys, CF3, CF3M, CF8, and CF8M, in pristine condition. Mechanical tests included uniaxial tensile tests, Charpy impact tests, and fracture toughness tests. Chemical analysis and microstructural examination were also performed for the same alloys. Further, CALPHAD calculation was performed to simulate phase stability and precipitation behaviors. The results of these baseline tests and analyses are summarized as follows:

[1] Relatively low ferrite volume fractions were measured: the volume fractions from optical micrographs were 7.9 and 6.7% for CF3 and CF8 and 11.8 and 11.6% for CF3M and CF8M, respectively. Elemental partitioning between ferrite and austenite were confirmed by EDS maps, which showed enrichment of Cr and Mo in ferrite and that of Ni in austenite, but nearly uniformly distributed Fe content.

[2] In the temperature range of -100 to 400 °C both ductility and strength decreased with test temperature. Very high tensile strength (>800 MPa) and high total ductility (>70%) were measured at the lowest test temperature, which might be because of highly linear dislocation slip, along with formation of twins and martensite particles.

[3] In aging temperature region (290-400 ºC) both the strength and the ductility were not temperature dependent, which might indicate that the same dislocation glide mechanism is responsible for the tensile deformation.

[4] The impact energy of model alloys showed clear but wide transition region in the test temperature range of -196 to 100ºC. The lower shelf of impact energy was not observed for any of the model alloys. The upper shelf was observed in the 0–100ºC region for CF3, CF8, and CF8M, but not for CF3M, which showed jamming between anvils due to excessive plasticity at 100 ºC (a 'no test' case).

[5] Since either or both of the energy shelves were not observed in the highly ductile model alloys, the ductile-brittle transition temperature (DBTT) could not be defined. A new index, T_{100J}, was defined for comparison of materials. The T_{100J} values determined on the impact energy transition curves were -125, -143, -118, and -175 ºC for CF3, CF3M, CF8, and CF8M, respectively.

[6] In the fracture test temperature range of -175 to 400 ºC the fracture mode of four model alloys was fully ductile with stable crack growth, and consequently very high fracture resistance (J-R) was measured in all test conditions. No fracture toughness (K_{JQ}) below 200 MPa√m was measured from the model alloys over the whole test temperature range.

[7] Peak fracture toughness was observed at RT or -100ºC, below which K_{JQ} decreased with temperature but never reached brittle or lower shelf region. Similar to the tensile ductility and strength, the variation of fracture toughness in the aging temperature region (290–400 ºC) was not significant.

[8] Simulation could provide valuable predictive information on the precipitation behavior of the model alloys: The G-phase formation is strongly dependent on aging temperature and is relatively enhanced in the CF3M and CF8 alloys. The Fe_2Mo Laves phase forms preferably in the high Mo alloys, CF3M and CF8M. The π-phase formed in the alloys with high Mo contents at the lowest aging temperature (290 ºC) only. The simple nitride (Cr_2N) and common carbide ($M_{23}C_6$) formed in all model alloys, but with a weak dependence on aging temperature.

REFERENCES

[1] T.S. Byun and J.T. Busby, "Cast Stainless Steel Aging Research Plan," report for Light Water Reactor Sustainability Program, ORNL/LTR-2012/440, September, 2012.

[2] G.F. Vander Voort, G.M. Lucas, and E.P. Manilova, Metallography and Microstructures of Stainless Steels and Maraging Steels, *Metallography and Microstructures,* Vol 9, *ASM Handbook,* ASM International, 2004, p. 670-700.

[3] O. K. Chopra and A. Sather, "Initial Assessment of the Mechanisms and Significance of Low–Temperature Embrittlement of Cast Stainless Steels in LWR Systems," NUREG/CR–5385 (ANL–89/17) (1990).

[4] H. M. Chung and T. R. Leax, "Embrittlement of Laboratory– and Reactor–Aged CF3, CF8, and CF8M Duplex Stainless Steels," *Mater. Sci. Technol.*, **6**, 249–262 (1990).

[5] H.M. Chung, "Evaluation of Aging of Cast Stainless Steel Components," *ASME Pressure Vessel & Piping Conference*, San Diego, CA, June 23-27, (1991).
[6] O. K. Chopra, "Estimation of Fracture Toughness of Cast Stainless Steels during Thermal Aging in LWR Systems," NUREG/CR–4513 (ANL–93/22) (1993).
[7] W.F. Michaud, P.T. Toben, W.K. Soppet, O.K. Chopra, "Tensile-Property Characterization of Thermally Aged Cast Stainless Steels," NUREG/CR-6142 (ANL-93/35) (1994).
[8] M.T. Anderson, S.L. Crawford, S.E. Cumblidge, K.M. Denslow, A.A. Diaz, S.R. Doctor, "Assessment of Crack Detection in Heavy-Walled Cast Stainless Steel Piping Welds Using Advanced Low-Frequency Ultrasonic Methods," NUREG/CR-6933, PNNL-16292, March 2007.
[9] H. Jang, S. Hong, C. Jang, J.G. Lee, "The effects of reversion heat treatment on the recovery of thermal aging embrittlement of CF8M cast stainless steels," *Materials and Design*, 56 (2014) 517–521.
[10] Y. Chen, B. Alexandreanu, and K. Natesan, "Crack Growth Rate and Fracture Toughness Tests on Irradiated Cast Stainless Steels," ANL-12/56. (2012)
[11] ASTM E8/E8M, "Standard Test Methods for Tension Testing of Metallic Materials." (2013)
[12] ASTM E23 "Standard Test Methods for Notched Bar Impact Testing of Metallic Materials," (2012)
[13] ASTM E1820 "Standard Test Method for Measurement of Fracture Toughness," (2001)
[14] Baek, J. H., Byun, T. S., Maloy, S. A., and Toloczko, M. B., "Investigation of Temperature Dependence of Fracture Toughness in High-Dose HT9 Steel Using Small-Specimen Reuse Technique," *Journal of Nuclear Materials*, 444 (2014) 206-213.
[15] Byun, T. S., Baek, J. H., Anderoglu, O, Maloy, S. A., and Toloczko, M. B., "Thermal Annealing Recovery of Fracture Toughness in HT9 Steel after Irradiation to High Doses," *Journal of Nuclear Materials*, 449 (1-3) (2014) 263-272.
[16] T.S. Byun, S.A. Maloy and J.H. Yoon, "Small Specimen Reuse Technique To Evaluate Fracture Toughness of High Dose HT9 Steel," *ASTM International (STP)*, accepted in 2014**.**
[17] S.M. Copley, B.H. Kear, "The dependence of the width of a dissociated dislocation on dislocation velocity," Acta Metallurgica, 16 (1968) 227.
[18] H.J. Kestenbach, "The Effect of Applied Stress on Partial Dislocation Separation and Dislocation Structure in Austenitic Stainless Steel," *Phil. Mag*. **36**, 1509 (1977).
[19] L.E. Murr, Interfacial phenomena in metals and alloys, Addision-Wesley Co. 1975.
[20] T.S. Byun, "On the stress dependence of partial dislocation separation and deformation microstructure in austenitic stainless steels," *Acta Materialia*, 51 (2003) 3063–3071.
[21] T.S. Byun, N. Hashimoto, K. Farrell, "Temperature dependence of strain hardening and plastic instability behaviors in austenitic stainless steels, Acta Materialia, 52 (2004) 3889–3899.
[22] L. Kaufman, B. Uhrenius, D. Birnie, K. Taylor, CALPHAD, 8, 25-66 (1984).
[23] Y. Yang and J.T. Busby, Journal of Nuclear Materials, 448 (s1-3),282-293 (2014).
[24] W. Cao, S.-L. Chen, F. Zhang, K. Wu, Y. Yang, Y. A. Chang, R. Schmid-Fetzer, W. A. Oates, CALPHAD, 33, 328-342 (2009).

[25] T. Sourmail, “Precipitation in creep resistant austenitic stainless steels,” *Materials Science and Technology*, 17 (2001) 1.

[26] K.H. Lo, C.H. Shek, J.K.L. Lai, “Recent developments in stainless steels,” *Mater Sci Engineer R* 65 (2009) 39-104.

[27] B. Weiss and R. Stickler, “Phase Instabilities during High Temperature Exposure of 316 Austenitic Stainless Steel,” *Metallurgical Transactions* 3 (1972) 851.

[28] J. Barcik, “Mechanism of σ-phase precipitation in Cr-Ni austenitic steels,” *Materials Science and Technology*, 4 (1988) 5-15.